Hindawi

Research Article

Structural and Optical Properties of Calcium Titanate Prepared from Gypsum

Massaud Mostafa [ID],[1,2] **Z. A. Alrowaili** [ID],[1] **M.M. Al Shehri** [ID],[1] **M. Mobarak** [ID],[1,3] **and Ahmed M. Abbas** [ID][4,5]

[1]*Physics Department, College of Science, Jouf University, Sakaka, Saudi Arabia*
[2]*Laser Technology & Environment Laboratory, Physics Department, Faculty of Science, South Valley University, Qena 83523, Egypt*
[3]*Physics Department, Faculty of Science, South Valley University, Qena 83523, Egypt*
[4]*Biology Department, College of Science, King Khalid University, Abha 61413, Saudi Arabia*
[5]*Department of Botany and Microbiology, Faculty of Science, South Valley University, Qena 83523, Egypt*

Correspondence should be addressed to Massaud Mostafa; mmostafa@ju.edu.sa

Ceramic materials have been used in various human health-related applications for considerable time. One of the important applications of ceramic materials is in electronics. Our work focuses on calcium titanate ($CaTiO_3$). $CaTiO_3$ is typically created via sintering. Gypsum particles is used to form calcium hydroxide, which is then combined with titanium dioxide to form rutile crystals. Thereafter, calcination is performed at 900°C, 1000°C, and 1100°C for 2 h. X-ray diffraction is employed to track the evolution of the $CaTiO_3$ phase. Scanning electron microscopy is used to characterize the morphologies of the different preparation steps. As the calcination temperature increases from 900°C to 1000°C, the crystallite size of $CaTiO_3$ increases from 35 nm to 45 nm. Furthermore, the energy gaps of the $CaTiO_3$ powders obtained after calcination at 900°C and 1000°C are 5.32 eV and 5.43 eV, respectively, and their particle sizes are 150–200 nm and 200–300 nm, respectively.

1. Introduction

The general formula of perovskites is ABO_3 (A is a rare or alkaline earth metal and B is a first-row transition metal). Calcium titanate ($CaTiO_3$), which is considered as the "founding father" of the perovskite family of titanium-based perovskite-type oxide photocatalysts [1–7], is attracting increasing attention. $CaTiO_3$ is a chemically stable *n*-type semiconductor with a broad bandgap of 3–3.5 eV [8]. Ca ions are located at the corners (1/2, 1/2, 1/2), Ti at the body center (0, 0, 0), and oxygen at the face center (1/2, 0, 0; 0, 12, 0; 0, 0, 1/2) [9]. $CaTiO_3$ is an alkaline earth metal titanate composed of earth-abundant nontoxic elements. It is fabricated using various methods [10], e.g., solid-state, coprecipitation, mechanochemical, sol-gel, hydrothermal, and solvothermal processes. Among these, the sol-gel process is

the most widely used method. $CaTiO_3$ exhibits excellent qualities as a multifunctional material, including optical properties, high dielectric constant, ferroelectricity, chemical stability, small dielectric loss, low cost, and environmental friendliness [11]. Several properties of $CaTiO_3$ have been explored owing to its broad applications. $CaTiO_3$ shows electrical properties when it is applied to electronic devices such as capacitors and thermistors. Hence, it has been extensively explored as an electroceramic material. In addition, it is known as a microwave ceramic owing to its dielectric response in the microwave spectrum. The photocatalytic activity and dynamic efficiency of $CaTiO_3$ have been investigated in decomposing organic dye waste in aquatic environments and water splitting for H_2 production, CO_2 reduction, and other applications. $CaTiO_3$ has been developed as an implant material for biomedical applications in

composites with hydroxyapatite [12]. Furthermore, it is a good substitute for the commercial titanium dioxide (TiO_2) catalyst in photocatalytic applications. The property of volume growth caused by water absorption is observed in rocks containing clay minerals and anhydrite. Rock swelling is a term used to describe this phenomenon. The origin of swelling in anhydrite is chemical, and it depends on the transformation of anhydrite into gypsum [13]. The solid-solid reaction of CaO or $Ca(OH)_2$ with TiO_2 at a specific molar content is the basic principle of the synthesis of $CaTiO_3$ perovskite material [14]. Calcium can be obtained from a low-cost source such as gypsum. Aside from the benefits of using gypsum as a low-cost calcium source, this research attempted to manufacture $CaTiO_3$ perovskite material from gypsum and test it on a laboratory scale as a simple and low-cost ceramic material.

The goal of this study was to synthesize $CaTiO_3$ using a sol-gel technique with calcium hydroxide ($Ca(OH)_2$) and TiO_2 as starting materials and ethanol as the dispersion medium. Gypsum rock samples were collected from a specified site in Gebel Elba National Park in southeastern Egypt, as shown in Figure 1, and $Ca(OH)_2$ was obtained from treated gypsum rocks. The gels disintegrated into $CaTiO_3$ precipitates. Crystalline $CaTiO_3$ powders were obtained by calcining the precipitate at 900°C, 1000°C, and 1100°C for 2 h. Transmission electron microscopy (TEM), X-ray diffraction (XRD), and scanning electron microscopy (SEM) were performed to study the microstructural and morphological behavior of dried $CaTiO_3$ sol-gel powders.

2. Materials and Methods

First, the raw material was collected from gypsum stones washed using distilled water and then ground with a heavy grinder. Next, the small stone pieces were milled using a ball-milling machine to obtain gypsum powder with the chemical formula of $CaSO_4.2H_2O$. Commercially available rutile titanium dioxide (TiO_2) was used to synthesize $CaTiO_3$ powders via combustion. Calcium sulfate ($CaSO_4$) powder was obtained by calcining the gypsum powder at 500°C to evaporate H_2O particles. Then, the powder was mixed with potassium hydroxide (KOH) for 1 h using a magnetic stirrer at a temperature of 80°C. The mixture was filtered to obtain $Ca(OH)_2$. Figure 2 shows the preparation steps.

The sol-gel method was used to produce $CaTiO_3$ powder from $Ca(OH)_2$ powder and TiO_2. These were added to distilled water and stirred for 2 h at 80°C to obtain all re-actants in the form of a gel. The gel was dried at 70°C for 20 h to obtain a powder, which was sintered at 900°C, 1000°C, and 1100°C for 2 h. The final powder was pressed into pellets and sintered at 1000°C. The powder samples were characterized using XRD, SEM, and TEM, as shown in Figure 3.

2.1. Measurements. All prepared particles were characterized by XRD. Particles were observed with a Zeiss LEO 912 OMEG operated at 100 kV accelerating voltage. Crystal structures of the particles were measured with an X-ray diffractometer (Rigaku RU-200A) operated at 40 kV and

30 mA with $CuK\alpha$ radiation using a monochromator. Optical properties of the nanoparticles were studied by a UV-visible spectrophotometer (UV2300II). The Fourier transmission infrared (FTIR) spectra of the samples were recorded by using FTIR (Shimadzu, model DF 803) in the wave range 400–4000 cm. Scanning electron microscopy (JEOL, JSM 5500LV) and transmission electron microscopy (JEOL, JEM 1010) were employed to reveal the microstructure of the synthesized powders, whereas the elemental analysis was studied using energy dispersive spectroscopy (Oxford Instruments, ISIS Link).

3. Results and Discussion

3.1. XRD Characterization. Figure 4 shows the XRD patterns obtained at different steps during the preparation of $CaTiO_3$. Broad XRD peaks suggest the presence of nanocrystalline particles. The XRD patterns were used to calculate the crystallite sizes and strain were using Scherrer's formula and the Williamson–Hall equation. The results are given in Table 1.

Figure 4(a) shows the XRD patterns of gypsum ($CaSO_4 \cdot 2H_2O$). XPert HighScore was used to analyze the XRD results to obtain the Miller indices and crystallographic parameters of mineral gypsum, as given in Table 1.

Figure 4(b) shows the XRD patterns for $CaSO_4$. The Match software was used to identify $CaSO_4$ peaks. Figure 4(c) shows the main compounds present in the three analyzed $Ca(OH)_2$ samples. The peaks are assigned to KOH (α) in addition to $Ca(OH)_2$. This may be because KOH and $CaSO_4$ did not fully react. This indicates that the reactants may need to be stirred for longer than 2 h. However, this step of the preparation was not returned because of the expectation that KOH will evaporate during calcination.

$$CaSO_4 + 2KOH \longrightarrow Ca(OH)_2 + K_2SO_4. \qquad (1)$$
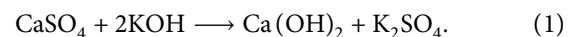
In this reaction, calcium sulfate joins with potassium hydroxide, a base. The OH^- from the base joins to form calcium hydroxide, while the SO_4^- and K^+ ions join to form potassium sulfate. A chemical filter paper is used to separate calcium hydroxide and remove potassium sulfate, as shown in Figure 2.

The XRD patterns were analyzed to assess the crystal structure. Figure 4(d) shows the XRD patterns of the $CaTiO_3$ powder produced after calcination at 900°C for 2 h. The diffraction patterns of $CaTiO_3$ are consistent with the JCPDS card (no. 22-0153). A few minor peaks (denoted by β) are caused by TiO_2 impurities, which are associated with an incomplete reaction. In addition, we assume an orthorhombic phase because of the Pbnm space group. The crystallographic variables obtained from the XRD analysis are given in Table 2.

The XRD patterns were analyzed to assess the crystal structure. Figure 4(e) shows the XRD results of the $CaTiO_3$ powder produced via calcination at 1000°C for 2 h. The diffraction patterns are consistent with the JCPDS card (no. 22-0153). Additionally, a few small peaks (denoted by β) are due to the presence of TiO_2 impurities, indicating an
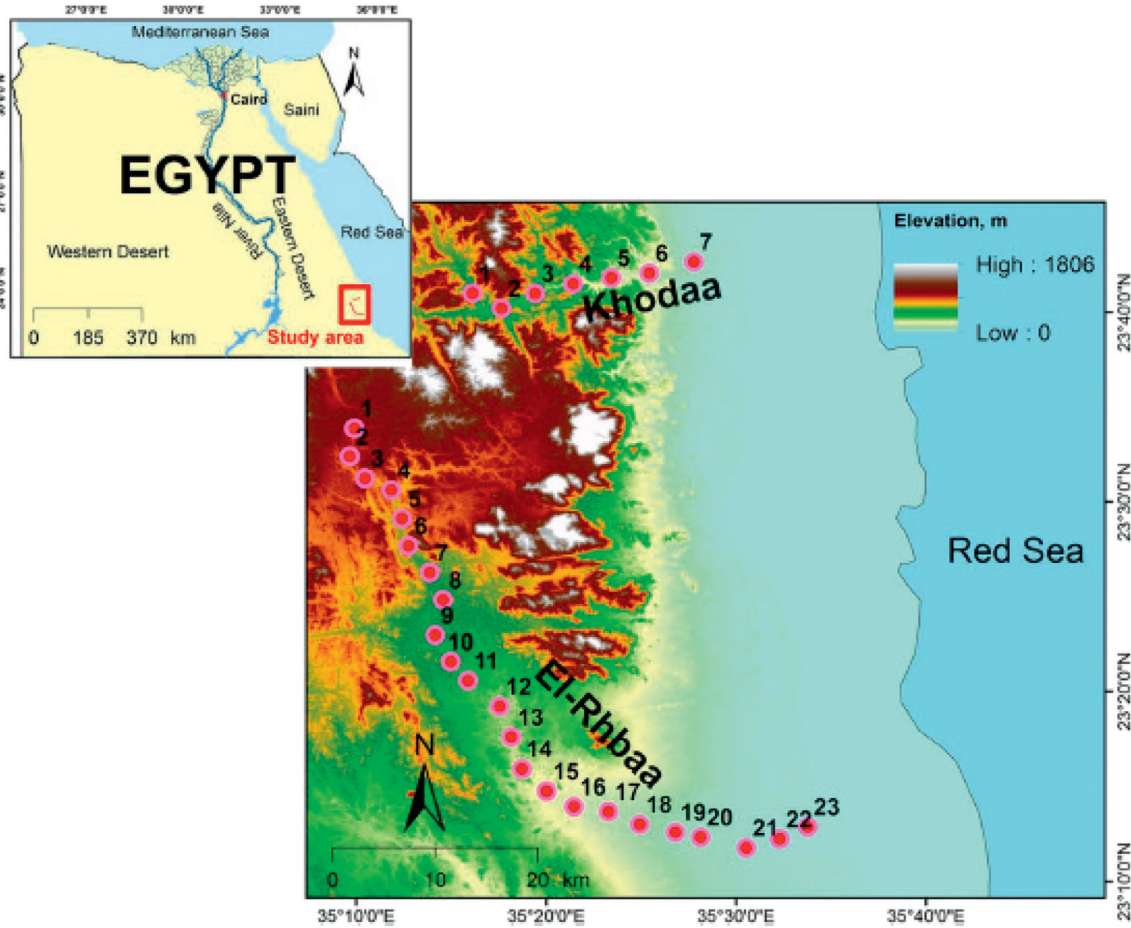
FIGURE 1: Site map of the collected gypsum samples (Gabal Elbah) [15].

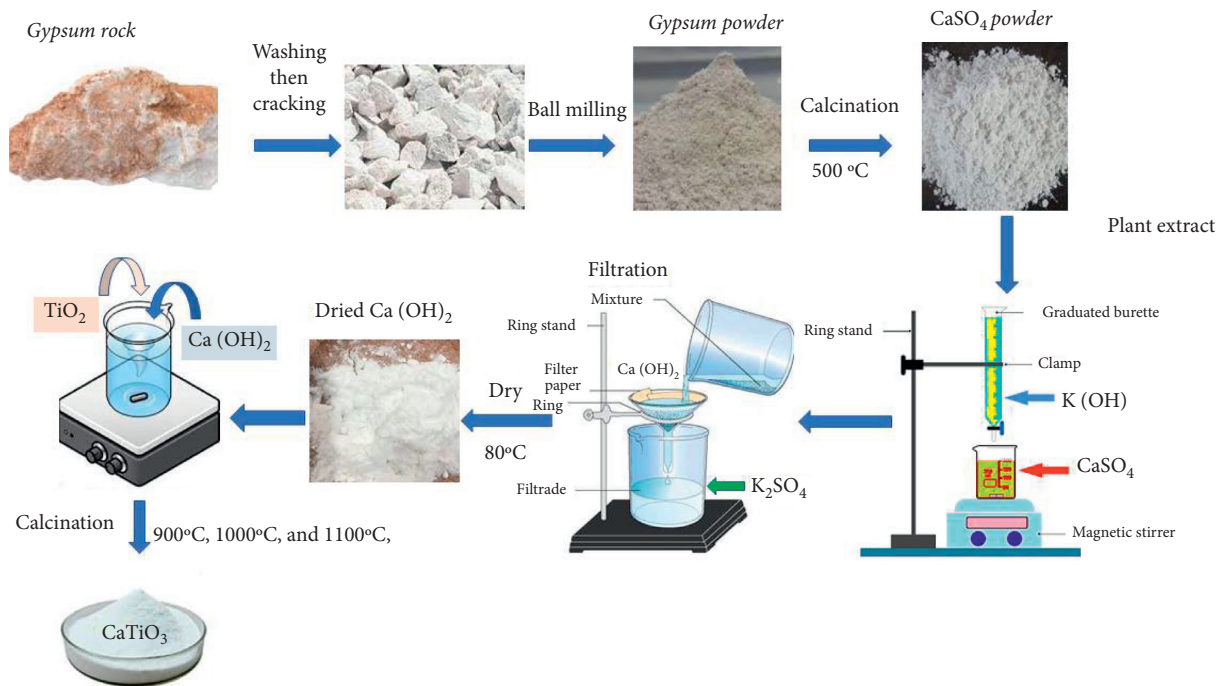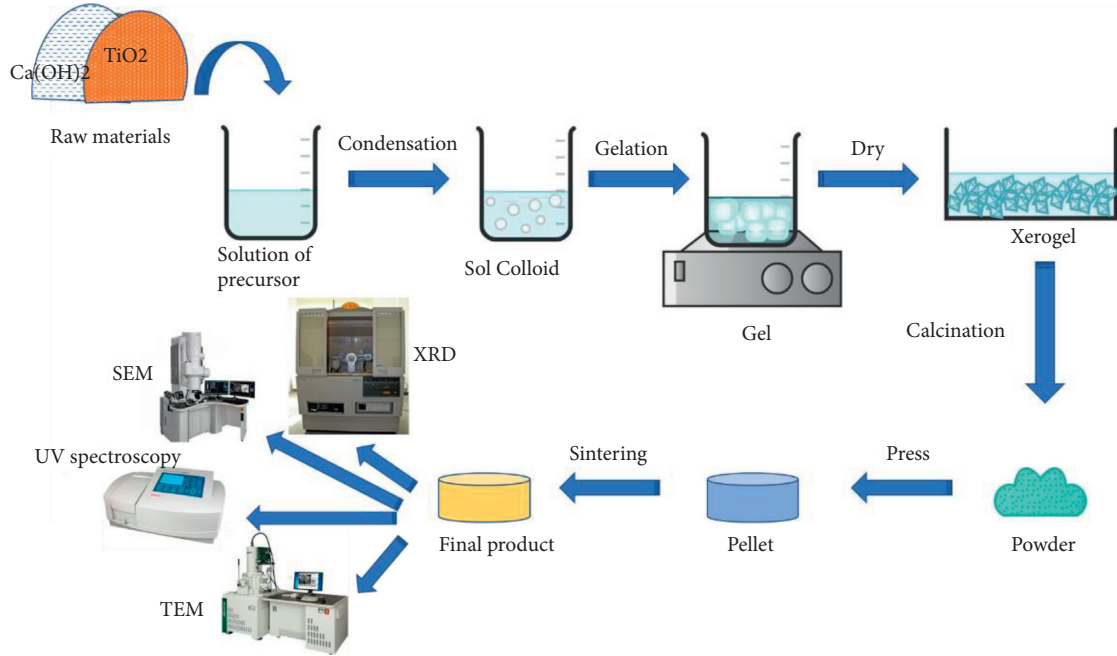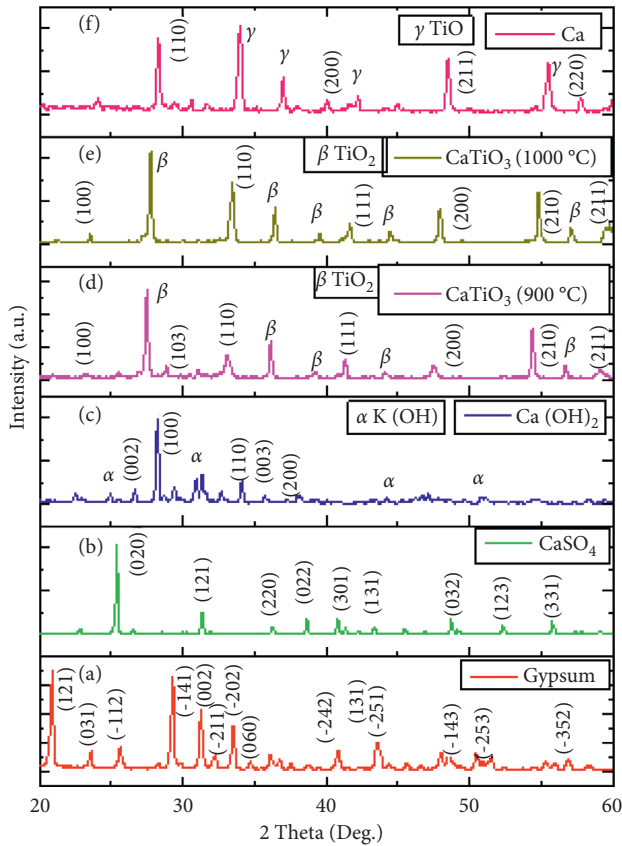FIGURE 2: Preparation of CaTiO$_3$ powders via the sol-gel technique.

FIGURE 3: Block diagram of the sol-gel preparation method.

FIGURE 4: XRD patterns obtained at different $CaTiO_3$ preparation steps.

TABLE 1: Crystal size values derived using the average Scherrer, Scherrer straight line, and Williamson–Hall methods.

Material	Scherrer (nm)	Williamson–Hall (nm)	Strain
$CaSO_4.2H_2O$	40	45.4	2.2×10^{-3}
$CaSO_4$	68.7	60	8.5×10^{-5}
$Ca(OH)_2$	39.9	40.2	1.5×10^{-3}
$CaTiO_3$ (900°C)	35.4	30.2	1.006×10^{-6}
$CaTiO_3$ (1000°C)	45.2	46	7.3×10^{-4}

Figure 4(f) shows the XRD patterns of the powder produced via calcination at 1100°C for 2 h. These patterns show that $CaTiO_3$ is not formed. This may be because the bonds between $Ca(OH)_2$ and TiO_2 are destroyed at a high temperature. The XRD patterns show calcium (Ca) ions and TiO. We can assume that the phase of the Ca ions is cubic with the Im-3m space group. The crystallographic parameters obtained from the XRD analysis are given in Table 2.

The expected reaction may be as follows:

$$Ca(OH)_2 + TiO_2 \longrightarrow Ca + TiO + 2H_2O\uparrow. \qquad (2)$$
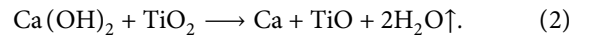
Understanding the tolerance factor aids in the development of novel perovskite compounds. Goldschmid's tolerance factor t was used to classify the synthesis of perovskite-type compounds:

$$t = \frac{r_{A+}r_O}{\sqrt{2}(r_B + r_O)}, \qquad (3)$$

where r_A, r_B, and r_O are the effective ionic radii of A and B sites and the oxygen ion sites, respectively, where $r_{Ca^{2+}} = 1.48$ Å, $r_{Ti^{4+}} = 0.745$ Å, and $r_{O^{2-}} = 1.21$ Å indicate radii values. A site and B site cations' bonding requirements

incomplete reaction. The Pbnm space group indicates the orthorhombic phase. The crystallographic parameters obtained from the XRD analysis are given in Table 2.

TABLE 2: Crystallographic parameters of different materials.

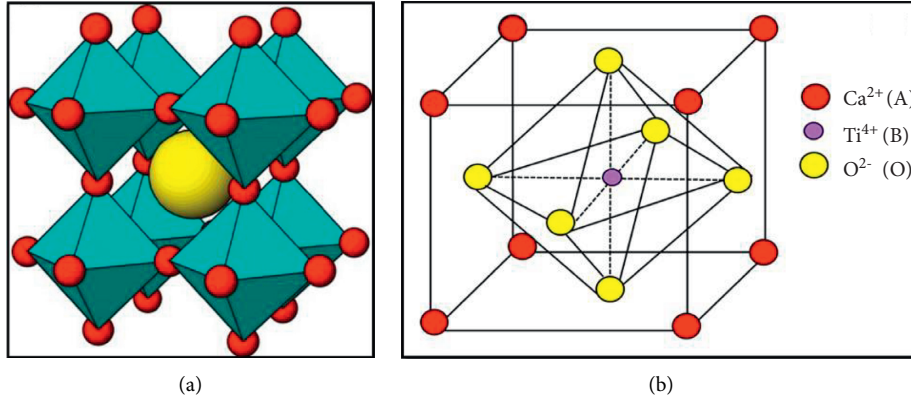| Material	Crystal system	Space group	Space group number	$a = b(\mathring{A})$	$c(\mathring{A})$	c/a	$\alpha = Y(°)$	$\beta(°)$
Gypsum	Monoclinic	$12/a$	15	5.6	6.51	1.16	90	118.4
CaSO$_4$	Orthorhombic	Bmmb	63	6.992	6.24	0.89	90	90
Ca(OH)$_2$	Orthorhombic	Bmmb	136	4.58	2.95	0.69	90	90
CaTiO$_3$ (900°C)	Orthorhombic	Pbnm	136	4.58	2.95	0.46	90	90
CaTiO$_3$ (1000°C)	Cubic	Im-3m	229	4.47	4.47	1	90	90

(a)　　　　　　　　　　　　　　　　　　(b)

FIGURE 5: (a) Ideal cubic perovskite structure for ABO3 (cyan, BO6 units; yellow, A atoms) (Reprinted with permission from reference [18]-[11] copyright from Elsevier). (b) Illustration of the crystal structure of CaTiO$_3$.

in the ABO3 perovskite is measured quantitatively by the tolerance factor which reflects the distortion structure that contains the octahedral rotation and tilt. As the substituent radii Ca^{2+} ion is at A site and radii Ti^{4+} ion at B site, the tolerance factor calculated values of the CaTiO$_3$ is 0.972. Hence, the general the structures tend to be in the perovskite structure as the calculated tolerance factor $t \sim 1$ [16].

The cubic structure of CaTiO$_3$ is shown in Figure 5(b), with Ca ions occupying the A site, Ti ions occupying the B site, and O representing the oxygen anion [17–19]. However, with CaTiO$_3$ calcined at 900 C, the perovskite structure deviates from cubic symmetry and transitions to orthorhombic phase, as given in Table 2, in order to fit the Ca^{2+} cations, which are smaller in size than the ideal ions for site "A." The tolerance factor is used to calculate the degree of distortion in the ideal cubic structure (t).

3.2. SEM Characterization. Figure 5(a) shows the SEM micrographs of gypsum powder; the particles are either rectangular or rod shaped. Figure 5(b) shows the SEM micrographs of Ca(OH)$_2$; the particles are either rectangular or rod shaped.

Figures 6(c) and 6(d) show the microstructures of CaTiO$_3$ obtained after calcination at 900°C and 1000°C, respectively. We can deduce that this substance appears foamy. The microstructures of the particles are almost nonexistent. All of the CaTiO$_3$ powders had an ultra-agglomeration powder, and because of the chemically active particles, they agglomerate quickly. This is why it was so difficult to achieve greater magnifications, as we had previously done with gypsum and calcium hydroxide samples,

where increased magnification resulted in visual blurring at higher magnifications.

3.3. TEM Characterization. Figures 7(a) and 7(b) show the TEM micrographs of CaTiO$_3$ powders obtained after calcination at 900°C and 1000°C, respectively, and a spherical morphology is observed. Figures 6(c) and 6(d) show the length distribution histograms of these powders. In the CaTiO$_3$ powder obtained after calcination at 900°C, the size of most particles is 150–200 nm, and there are a few agglomerated particles. The average particle size of the CaTiO$_3$ powder obtained after calcination at 1000°C is 200–300 nm.

3.4. Optical Properties. The UV-vis absorbance spectra (at room temperature) of CaTiO$_3$ powders are shown in Figure 8. The wavelength of the spectra is 200–800 nm. The absorption decreases rapidly for a wavelength of 200–250 nm but remains almost constant for 250–800 nm.

Wood and Tauc [20] demonstrated the relationship between the absorption curve and energy gap of a material. The bandgap values were obtained by extrapolating the linear region of the curve. According to this method, the energy dependence of the gap and optical absorbance can be expressed as follows:

$$hv\alpha = \left(hv - E_g^{opt}\right)^2, \tag{4}$$

where α is the absorbance, h is Planck's constant, m is the frequency, and E_g^{opt} is the bandgap of a material.

(a)

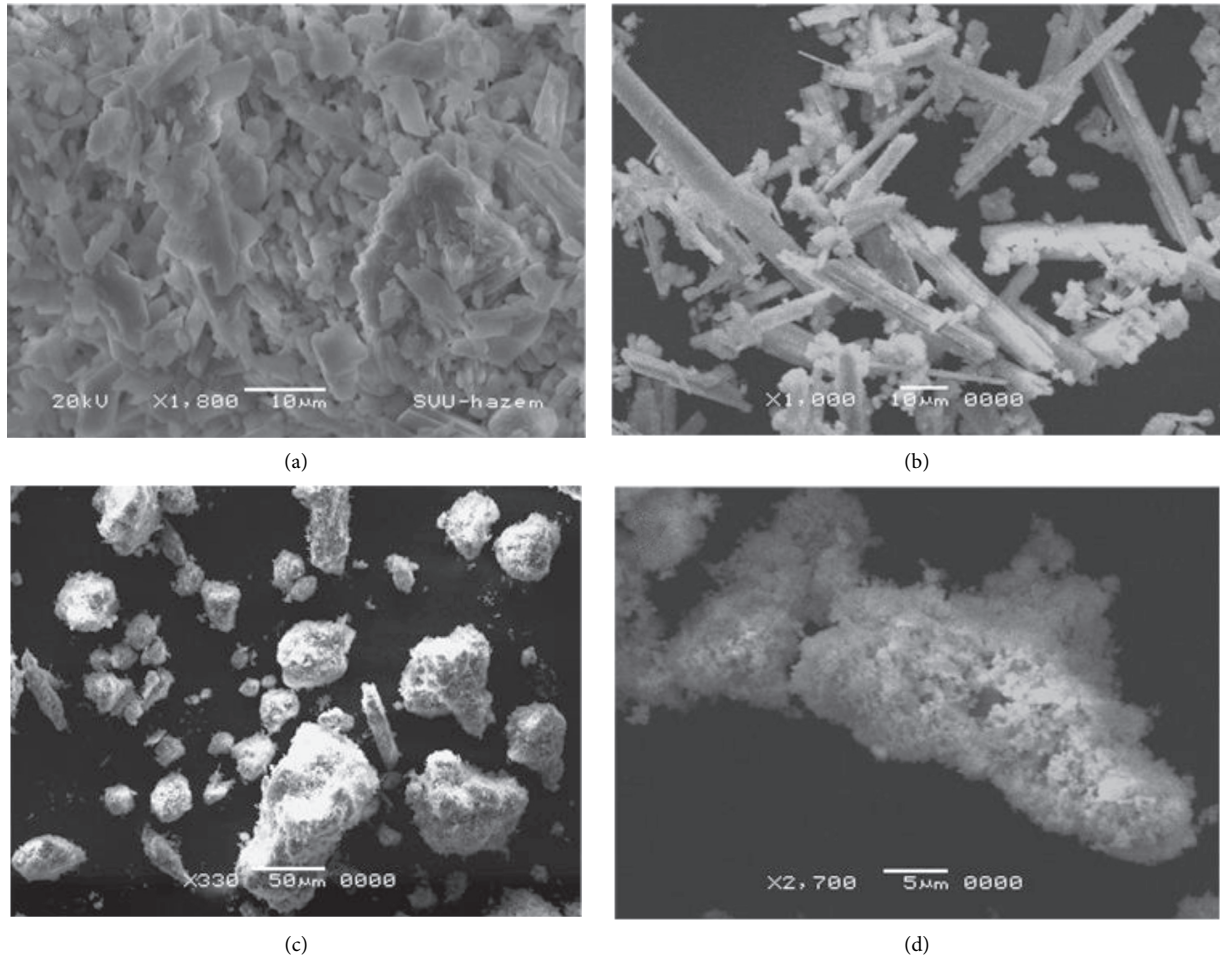(b)

(c)

(d)

FIGURE 6: SEM micrograph of (a) gypsum, (b) Ca(OH)$_2$, (c) CaTiO$_3$ obtained after calcination at 900°C, and (d) CaTiO$_3$ obtained after calcination at 1000°C.

(a)

(b)
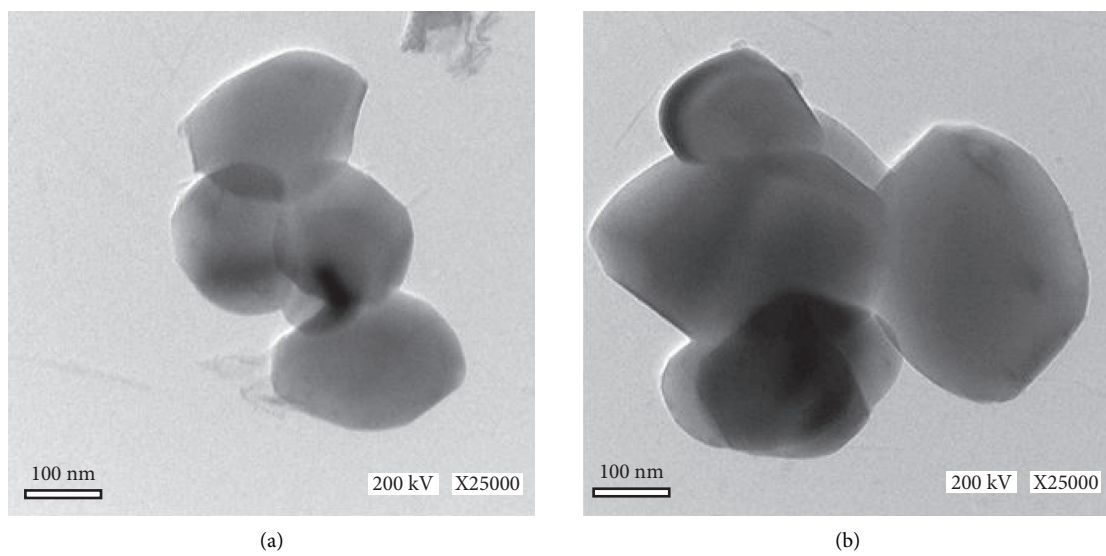
FIGURE 7: Continued.

(c)

(d)
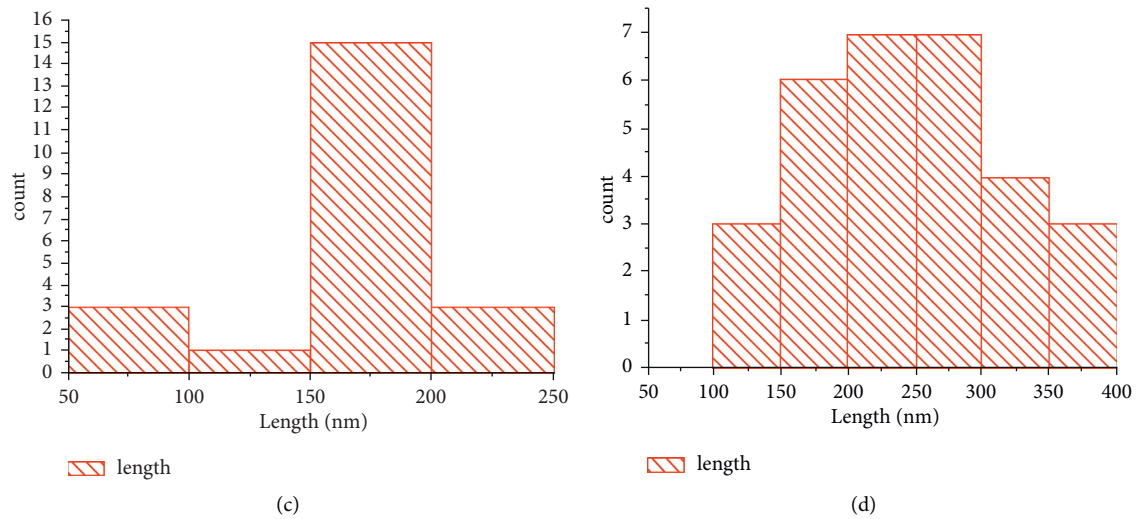
FIGURE 7: TEM micrographs of CaTiO$_3$ obtained after calcination at (a) 900°C and (b) 1000°C. Length distribution histograms of CaTiO$_3$ obtained after calcination at (c) 900°C and (d) 1000°C.
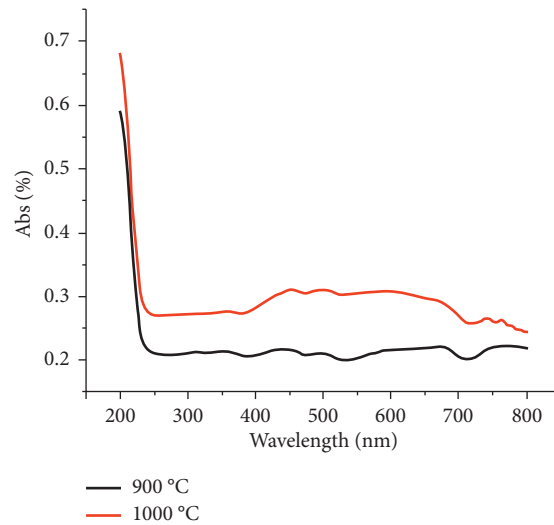
FIGURE 8: UV-vis absorbance spectra of CaTiO$_3$ obtained after calcination at 900°C and 1000°C.
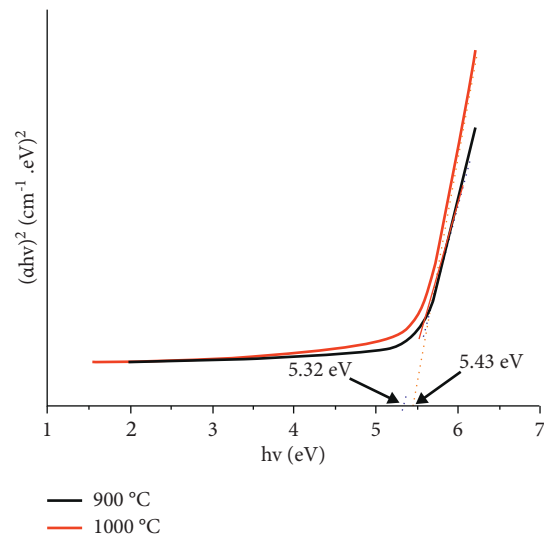
FIGURE 9: Energy gaps for CaTiO$_3$ obtained after calcination at 900°C and 1000°C.
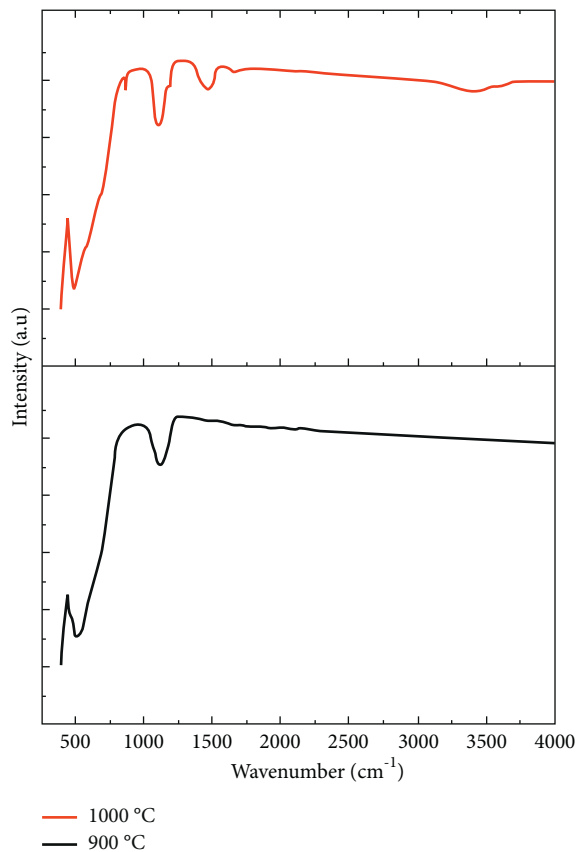
Figure 10: FTIR spectra of $CaTiO_3$ obtained after calcination at 900°C and 1000°C.

Figure 9 shows the calculated bandgaps for $CaTiO_3$ powders obtained after calcination at 900°C and 1000°C, which are 5.32 and 5.43 eV, respectively.

E_{gap} values were measured in previous research, and the results were calculated by extrapolating the linear section of the curve using linear regression to arrive at E_{gap} values of about 3.51 eV [21]. An increase in the bandgap may be identified for the current $CaTiO_3$ when compared to previous works, which can be due to the existence of TiO_2 secondary phase, which can cause defects such as distortions along CaO linkages, which result in localized electronic levels in the band gap.

3.5. *Fourier-Transform Infrared Spectroscopy Analysis.* Fourier-transform infrared spectroscopy (FTIR) analyses were performed for $CaTiO_3$ powders obtained after calcination at 900°C and 1000°C. The results are shown in Figure 10. The band at 570 cm^{-1} is assigned as the signature peak of the $CaTiO_3$ bond. The absorption peak at 460 cm^{-1} is due to the bending mode of the Ti-O-Ti bond. The absorption peak at 567 cm^{-1} is characterized as Ti-O stretching vibration. This implies the existence of TiO_6 octahedra and the formation of a $CaTiO_3$ perovskite-type structure [22]. For the $CaTiO_3$ powder obtained at 1000°C, the broad bands observed above 3644 cm^{-1} and 3429 cm^{-1} are related to the superposition of the vibration band of the hydroxyl group and the stretching vibration of the adsorbed OH group.

4. Conclusions

$CaTiO_3$ was successfully prepared from gypsum using a sol-gel method and characterized via TEM, XRD, and SEM. XRD analysis confirmed the presence of the pure crystalline $CaTiO_3$ phase after calcination at 900°C and 1000°C for 2 h, along with unreacted TiO_2 particles. According to TEM observations, the $CaTiO_3$ powder obtained after calcination at 900°C had a particle size of 150–200 nm and exhibited agglomeration of nanoparticles. The $CaTiO_3$ powder obtained after calcination at 1000°C had a particle size of 200–300 nm. SEM observations showed that $CaTiO_3$ particles did not have a specific microstructure. The energy gaps for $CaTiO_3$ powders obtained after calcination at 900°C and 1000°C were 5.32 eV and 5.43 eV, respectively. Infrared bands were analyzed to identify the functional groups of $CaTiO_3$. The bands at approximately 570 cm^{-1} were due to the signature peak of the $CaTiO_3$ bond. The band at 567 cm^{-1} was due to Ti-O stretching vibration. Furthermore, the bands close to 460 cm^{-1} were attributed to the Ti-O-Ti bending mode.

Data Availability

Data collected from the literature can be consulted in the relevant articles; the authors' data are available upon request to Dr. Massaud Mostafa at mmostafa@ju.edu.sa.

Conflicts of Interest

The authors declare that they have no conflicts of interest.

Acknowledgments

References

[1] R. Acharya and K. Parida, "A review on TiO_2/g-C_3N_4 visible-light- responsive photocatalysts for sustainable energy generation and environmental remediation," *Journal of Environmental Chemical Engineering*, vol. 8, no. 4, Article ID 103896, 2020.

[2] P. A. Owusu and S. Asumadu-Sarkodie, "A review of renewable energy sources, sustainability issues and climate change mitigation," *Cogent Engineering*, vol. 3, no. 1, Article ID 1167990, 2016.

[3] K. Qi, B. Cheng, J. Yu, and W. Ho, "A review on TiO_2-based Z-scheme photocatalysts," *Chinese Journal of Catalysis*, vol. 38, no. 12, pp. 1936–1955, 2017.

[4] L. Finegold and J. L. Cude, "Biological sciences: one and two-dimensional structure of alpha-helix and beta-sheet forms of poly(L-alanine) shown by specific heat measurements at low

temperatures (1.5-20 K)," *Nature*, vol. 238, no. 5358, pp. 38–40, 1972.

[5] H. Wang, L. Zhang, Z. Chen et al., "Semiconductor heterojunction photocatalysts: design, construction, and photocatalytic performances," *Chemical Society Reviews*, vol. 43, no. 15, pp. 5234–5244, 2014.

[6] J. Wen, X. Li, W. Liu, Y. Fang, J. Xie, and Y. Xu, "Photocatalysis fundamentals and surface modification of TiO_2 nanomaterials," *Chinese Journal of Catalysis*, vol. 36, no. 12, pp. 2049–2070, 2015.

[7] A. Kumar, C. Schuerings, S. Kumar, A. Kumar, and V. Krishnan, "Perovskite-structured $CaTiO_3$ coupled with g-C_3N_4 as a heterojunction photocatalyst for organic pollutant degradation," *Beilstein Journal of Nanotechnology*, vol. 9, pp. 671–685, 2018.

[8] L. H. Oliveira, A. P. De Moura, F. A. La Porta et al., "Influence of Cu-doping on the structural and optical properties of $CaTiO_3$ powders," *Materials Research Bulletin*, vol. 81, pp. 1–9, 2016.

[9] M. Rizwan, Z. Usman, M. Shakil et al., "Electronic and optical behaviour of lanthanum doped $CaTiO_3$ perovskite," *Materials Research Express*, vol. 7, no. 1, p. 015920, Article ID 015920, 2020.

[10] M. M. Maroneze, L. Q. Zepka, J. G. Vieira, M. I. Queiroz, and E. Jacob-Lopes, "A tecnologia de remoção de fósforo: gerenciamento do elemento em resíduos industriais," *Ambiente & Água-An Interdisciplinary Journal of Applied Science*, vol. 9, pp. 445–458, 2014.

[11] C. Karthikeyan, M. Thamima, and S. Karuppuchamy, "Structural and photocatalytic property of CaTiO3 nanosphere," *Materials Science Forum*, vol. 979, pp. 169–174, 2020.

[12] A. K. Dubey, B. Basu, K. Balani, R. Guo, and A. S. Bhalla, "Multifunctionality of perovskites BaTiO3 and CaTiO3 in a composite with hydroxyapatite as orthopedic implant materials," *Integrated Ferroelectrics*, vol. 131, no. 1, pp. 119–126, 2011.

[13] K. Kovári, C. Amstad, and G. Anagnostou, "Design/construction methods–tunneling in swelling rocks, key questions in rock mechanics," in *Proceedings of the 29th U.S. Key Questions in Rock Mechanics Symposium*, P. A. Cundall, R. L. Sterling, and A. M. Starfield, Eds., Balkema, Minneapolis, MN, USA, 13–15 June 1988.

[14] G. S. Kaliaraj, K. Kirubaharan, G. Pradhaban, P. Kuppusami, and V. Vishwakarma, "Isolation and characterization of biogenic calcium carbonate/phosphate from oral bacteria and their adhesion studies on YSZ-coated titanium substrate for dental implant application," *Bulletin of Materials Science*, vol. 39, no. 2, pp. 385–389, 2016.

[15] A. M. Abbas, M. Al-Kahtani, S. J. Novak, and W. S. Soliman, "Abundance, distribution, and growth characteristics of three keystone Vachellia trees in Gebel Elba National Park, south-eastern Egypt," *Scientific Reports*, vol. 11, no. 1, p. 1284, 2021.

[16] M. Mostafa, Z. A. Alrowaili, G. M. Rashwan, and M. K. Gerges, "Ferroelectric behavior and spectroscopic properties of La-modified lead titanate nanoparticles prepared by a sol-gel method," *Heliyon*, vol. 6, no. 2, Article ID e03389, 2020.

[17] P. Kanhere and Z. Chen, "A review on visible light active perovskite-based photocatalysts," *Molecules*, vol. 19, no. 12, pp. 19995–20022, 2014.

[18] J. Shi and L. Guo, "ABO3-based photocatalysts for water splitting," *Progress in Natural Science: Materials International*, vol. 22, no. 6, pp. 592–615, 2012.

[19] G. Zhang, G. Liu, L. Wang, and J. T. S. Irvine, "Inorganic perovskite photocatalysts for solar energy utilization," *Chemical Society Reviews*, vol. 45, no. 21, pp. 5951–5984, 2016.

[20] J. Tauc, "Optical properties of amorphous semiconductors," in *Amorphous and Liquid Semiconductors*, J. Tauc, Ed., Springer US., Boston, MA, USA, pp. 159–220, 1974.

[21] L. H. Oliveira, J. Savioli, A. P. de Moura et al., "Investigation of structural and optical properties of CaTiO3 powders doped with Mg^{2+} and Eu^{3+} ions," *Journal of Alloys and Compounds*, vol. 647, pp. 265–275, 2015.

[22] S. A. U. Portia, R. Srinivasan, E. Elaiyappillai, P. M. Johnson, and K. Ramamoorthy, "Facile synthesis of Eu-doped CaTiO3 and their enhanced supercapacitive performance," *Ionics*, vol. 26, no. 7, pp. 3543–3554, 2020.